

Magnetic-field-induced ab -plane rotation of the Eu magnetic moments in trigonal EuMg_2Bi_2 and EuMg_2Sb_2 single crystals below their Néel temperatures

Santanu Pakhira,¹ Yongbin Lee,¹ Liqin Ke,¹ and D. C. Johnston^{1,2}

¹*Ames Laboratory, Iowa State University, Ames, Iowa 50011, USA*

²*Department of Physics and Astronomy, Iowa State University, Ames, Iowa 50011, USA*

(Dated: August 15, 2022)

The thermodynamic and electronic-transport properties of trigonal EuMg_2Bi_2 in ab -plane magnetic fields \mathbf{H}_x and the A-type antiferromagnetic structure have recently been reported. The Eu magnetic moments with spin $S = 7/2$ remain locked in the ab plane up to and above the ab -plane critical field $\mathbf{H}_x^c = 27.5$ kOe at which the Eu moments become parallel to \mathbf{H}_x . Here additional measurements at low fields are reported that reveal a new spin-reorientation transition at a field $H_{c1} \approx 465$ Oe where the Eu moments remain in the ab plane but become perpendicular to H_x . At higher fields, the moments cant towards the field resulting in $M \propto H_x$ up to \mathbf{H}_x^c . Similar results are reported from measurements of the magnetic properties of EuMg_2Sb_2 single crystals, where $H_{c1} \approx 220$ Oe is found. Theory is formulated that models the low-field magnetic behavior of both materials, and the associated anisotropies are calculated. The ab -plane trigonal anisotropy in EuMg_2Sb_2 is found to be significantly smaller than in EuMg_2Bi_2 .

I. INTRODUCTION

The topological band properties have recently been investigated in crystallographically-ordered stoichiometric compounds because these properties are not as affected by disorder that occurs in substitutional solid solutions. Of particular interest here are the trigonal compounds EuMg_2Bi_2 and EuMg_2Sb_2 [1, 2] that can be cleanly grown as single crystals from self-fluxes [3]. The bands in EuMg_2Bi_2 have been studied [4], but not below the antiferromagnetic (AFM) ordering temperature $T_N \approx 7$ K [3] of this compound. The topological band structures of the nonmagnetic analogues YbMg_2Bi_2 and CaMg_2Bi_2 have also been investigated, where they are found to host topological surface states near the Fermi energy [5].

The low-temperature properties of EuMg_2Bi_2 have been studied in detail [3, 6, 7]. The magnetic structure below $T_N = 6.7(1)$ K is an A-type AFM structure, in which the Eu moments with spin $S = 7/2$ and spectroscopic splitting factor $g = 2$ are ferromagnetically aligned parallel to an Eu layer of the structure, whereas the moments in adjacent layers along the c axis are aligned antiparallel. The specific heat C_p exhibits a λ -type anomaly at T_N and short-range magnetic order at temperatures T above T_N . The magnetic entropy $\approx R \ln(8)$ at $T \gg T_N$ is consistent with that expected for Eu^{2+} magnetic moments with magnitude $\mu = gS \mu_B = 7 \mu_B$ with $g = 2$ and spin $S = 7/2$, where μ_B is the Bohr magneton. The ab -plane electrical resistivity $\rho_{ab}(T)$ exhibits metallic character with a mild and disorder-sensitive upturn below ~ 23 K.

The crystal structure and magnetic properties of polycrystalline EuMg_2Sb_2 have also been studied [1]. This compound contains Eu^{2+} ions that exhibit AFM order below $T_N = 8.2(3)$ K with Curie-Weiss behavior in the magnetic susceptibility χ above T_N . The ^{151}Eu Mössbauer spectra are consistent with this Eu^{2+} oxidation state. The band structure of EuMg_2Sb_2 was also reported. Detailed measurements of the magnetic

and thermal properties of EuMg_2Sb_2 single crystals have also been carried out recently [8]. The $\rho(T)$ and angle-resolved photoemission (ARPES) measurements revealed semiconducting behavior with an energy gap of 370 meV. The Eu^{2+} magnetic moments exhibit A-type AFM order below $T_N = 8.0(2)$ K. An additional second-order transition of unknown origin occurs in the $\chi_{ab}(T)$ data at 3.0 K.

EuMg_2Bi_2 and EuMg_2Sb_2 crystals showed puzzling features in the field-dependent ab -plane magnetic susceptibility $\chi_{ab}(T)$ below T_N . For EuMg_2Bi_2 , The $\chi(T < T_N)$ measurements for $H \parallel ab$ and $H \parallel c$ in a field of 1 kOe were the same (isotropic) [3], whereas for A-type AFM order one instead expects from molecular-field theory (MFT) that $\chi_{ab}(T \rightarrow 0) = \chi(T_N)/2$ and $\chi_c(T \rightarrow 0) = \chi(T_N)$ [9–11]. The authors of Ref. [3] suggested that this observed behavior arises from c -axis magnetic ordering instead of the above A-type ab -plane ordering subsequently reported [7]. Similarly, the data for $\chi_{ab}(T \leq T_N)$ in Ref. [6] for $H = 0.5$ –30 kOe were nearly independent of T . These authors suggested that this T -independent $\chi_{ab}(T \leq T_N)$ behavior might arise from a field-induced helical magnetic structure with a turn angle of $\approx 120^\circ$ based on MFT [9], which we now know is not the correct magnetic structure [7]. A similar anomalous behavior of $\chi_{ab}(H, T)$ was recently observed for EuMg_2Sb_2 crystals [8].

The above behavior of $\chi_{ab}(T \leq T_N)$ is correlated with anomalous low-field $M_{ab}(H)$ behavior for both EuMg_2Bi_2 and EuMg_2Sb_2 . For these materials, these data show an unexpected positive curvature as shown in Fig. 1 [7, 8]. It was suggested that this behavior may be caused by a field-induced reorientation of the magnetic moments in the three trigonal domains dictated by the crystal symmetry rather than by a field-induced change in the magnetic structure [7]. Here we test this hypothesis and find strong evidence for it using a new theory for magnetic-moment reorientation within the three trigonal domains

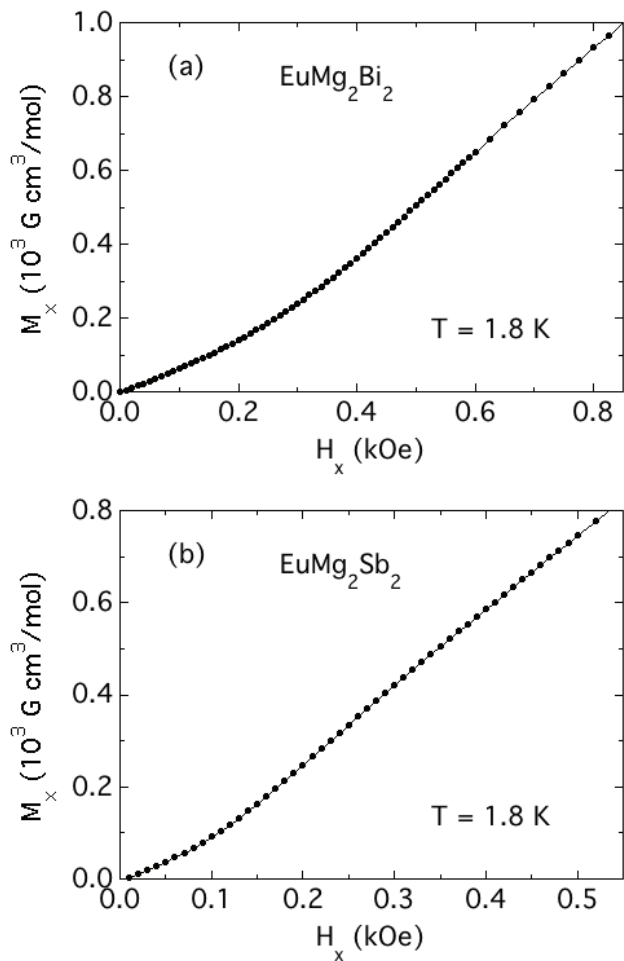


FIG. 1. Magnetization M versus magnetic field H_x applied in the ab plane of single-crystal (a) EuMg_2Bi_2 and (b) EuMg_2Sb_2 . A distinct positive curvature is observed for EuMg_2Bi_2 below ~ 500 Oe and for EuMg_2Sb_2 below ~ 200 Oe [7, 8].

in an ab -plane magnetic field.

The experimental and theoretical details are given in the following Sec. II. The theory for fitting the low-field $M_{ab}(H)$ data in Fig. 1 is presented in Sec. III. Fits to the data by the theory and calculations of the magnetic-dipole and magnetocrystalline anisotropies and comparisons with the fitted values are given in Sec. IV. Concluding remarks are given in Sec. V.

II. EXPERIMENTAL AND THEORETICAL DETAILS

Trigonal EuMg_2Bi_2 single crystals with room-temperature hexagonal lattice parameters $a = 4.7724(3) \text{ \AA}$ and $c = 7.8483(5) \text{ \AA}$ were grown by a self-flux method with starting composition EuMg_4Bi_6 as reported earlier [6, 7]. EuMg_2Sb_2 single crystals with room-temperature hexagonal lattice parameters $a = b = 4.6861(3) \text{ \AA}$ and $c = 7.7231(5) \text{ \AA}$ were also grown using self-flux with starting composition

$\text{EuMg}_4\text{Sb}_{16}$ [8]. The magnetization measurements were carried out using a Magnetic Properties Measurement System (MPMS, Quantum Design, Inc.) operating in the temperature range 1.8–300 K and with magnetic fields H up to 5.5 T (1 T = 10^4 Oe). For measurements with the field applied in the ab plane, the magnetic field was perpendicular to the [100] direction of the hexagonal unit cell as determined from Laue x-ray diffraction measurements, whereas in Ref. [6] the field was applied in an arbitrary direction in the ab plane.

Two contributions to the magnetic anisotropy (MA), magnetic-dipole anisotropy (MDA) and magnetocrystalline anisotropy (MCA), are calculated and compared to experiments. MDA energies (MDAE) K_D are calculated by a direct lattice summation over Eu atoms in a sufficiently large sphere to ensure convergence. MCA energies (MCAE) K are calculated using density functional theory (DFT) as implemented in Vienna *ab initio* simulation package (VASP) [12, 13]. We calculate the total energies of AFM A-type and FM orderings with different spin orientations. The MCAE of a particular magnetic ordering is calculated as

$$K = E_{001} - E_{100}, \quad (1)$$

where E_{001} and E_{100} are the total energies for the magnetization oriented along the [001] and [100] directions, respectively. Positive (negative) K corresponds to easy-plane (easy-axis) anisotropy. To decompose the MCAE, we also evaluate the on-site SOC energy $\langle V_{\text{so}} \rangle$ and the corresponding anisotropy

$$K_{\text{so}} = \frac{1}{2} \langle V_{\text{so}} \rangle_{001} - \frac{1}{2} \langle V_{\text{so}} \rangle_{100}. \quad (2)$$

As shown later, we found $K_{\text{so}} \approx K$, which is expected from the second-order perturbation theory [14, 15]. However, unlike K , K_{so} can be decomposed into sites, spins, and orbital pairs, providing an understanding of the MCA mechanism in a system [14–17].

The experimental crystal structures [6, 8] are used in all calculations. The nuclei and core electrons are described by the projector augmented-wave potential [18], and the wave functions of valence electrons are expanded in a plane-wave basis set with a cutoff energy of up to 520 eV. The spin-orbit coupling (SOC) is included using the second-variation procedure [19, 20]. In addition, the Hubbard Coulomb interaction $U = 6 \text{ eV}$ is included for better accounting for the strong correlation of Eu-4*f* electrons [21]. The k -point integration was performed using a modified tetrahedron method with Blöchl corrections. A $16 \times 16 \times 4$ k -point mesh is used for MCAE calculations to ensure sufficient convergence.

III. THEORY

A. Overview

As discussed later, EuMg_2Bi_2 and EuMg_2Sb_2 have a strong XY anisotropy which keeps the ordered moments confined to the trigonal ab plane for magnetic

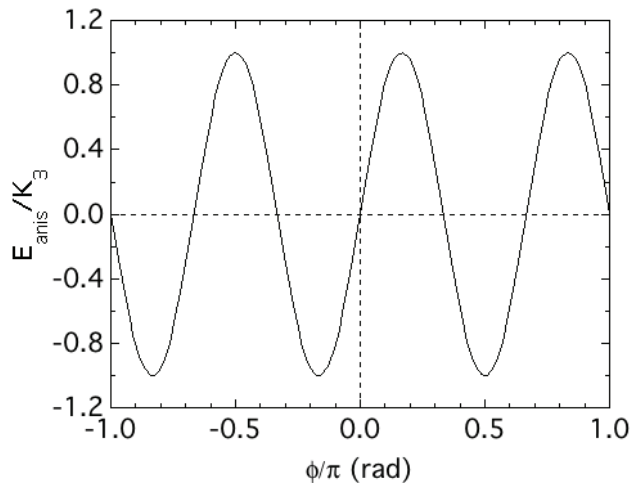


FIG. 2. In-plane trigonal anisotropy energy E_{anis} normalized by the anisotropy constant K_3 of a moment versus its angle ϕ with respect to the positive x axis. The three minima of E_{anis} are at $\phi/\pi = -5/6, -1/6,$ and $1/2$.

field applied parallel to this plane. The ab -plane trigonal anisotropy energy has the form

$$E_{\text{anis}} = K_3 \sin(3\phi), \quad (3)$$

where K_3 is the positive trigonal anisotropy constant and ϕ is the angle of a magnetic moment with respect to the positive x axis, which is the direction of the applied field \mathbf{H}_x . A plot of E_{anis} normalized by K_3 versus ϕ/π is shown in Fig. 2, where the angles ϕ of the negative anisotropy-energy minima with respect to the in-plane x axis are given in the figure caption. In $H = 0$, these are the angles of the moments in each domain as illustrated in Fig. 3(a) with $\Delta\phi = 0$. In $H = 0$, each domain contains two moments at 180° with respect to each other, where the two moments are respectively in alternating layers along the c axis of the A-type AFM structure. As shown, moments 1 and 2 are in Domain A, 3 and 4 are in Domain B, and 5 and 6 are in Domain C. The moments in different domains are assumed not to interact.

There is a small field $H_x \equiv H_{c1}$ at which the moments in all three domains become almost perpendicular to H_x as shown in Fig. 3(b), where we eventually determine $H_{c1} = 465$ Oe and 220 Oe for EuMg_2Bi_2 and EuMg_2Sb_2 , respectively (see Fig. 1). The tilt angle ϕ_{tilt} in a field H_x of each of the two moments in each domain at H_{c1} is given by $\phi_{\text{tilt}} = \arcsin(H_x/H_{ab}^c)$, where H_{ab}^c is the critical field in the ab plane at which all moments become parallel to H_x . Using $H_{c1} = 465$ Oe and $H_{ab}^c = 27,500$ Oe for EuMg_2Bi_2 , the tilt angle at H_{c1} is $\phi_{\text{tilt}} = 0.75^\circ$ at $H_x = H_{c1}$ which gives rise to the x -axis magnetization observed at that field. This tilt angle is negligible compared to the value of 90° at saturation. Thus for fields less than H_{c1} , we can consider the two moments in each domain to be (almost) locked at angles of $\approx 180^\circ$ to each other as shown by the arrows in Fig. 3(a).

The reason for the small value of ϕ_{tilt} is that the anisotropy energy is much smaller than the exchange interaction energy between the two spins in each domain which tends to keep them aligned antiparallel. For example, the ab -plane trigonal anisotropy parameter in EuMg_2Bi_2 according to Eq. (12a) below is $K_3 = 6.5 \times 10^{-8}$ eV/Eu, whereas the Heisenberg exchange interaction between a spin in one ferromagnetically-aligned layer and the spins aligned in the opposite direction in one of the two nearest layers is $J_1 = 1.97 \times 10^{-5}$ eV [6].

B. $0 \leq H_x \leq H_{c1}$

In the small fields $0 \leq H_x \leq H_{c1}$, the angles of the locked moments in domains A, B, and C in Fig. 3(a) with respect to the positive x axis are respectively given by

$$\begin{aligned} \phi_A &= \frac{\pi}{2}, \\ \phi_B &= -\frac{5\pi}{6} + \Delta\phi \quad (0 \leq \Delta\phi \leq \pi/3), \\ \phi_C &= -\frac{\pi}{6} - \Delta\phi. \quad (0 \leq \Delta\phi \leq \pi/3), \end{aligned} \quad (4)$$

where the magnitude of the angle of the moments in Domains B and C with respect to their initial angles is $\Delta\phi$. This is not the angle ϕ_{tilt} between the two locked moments in a domain discussed above. The anisotropy energy averaged over the moments in the three domains in the field range $0 \leq H_x \leq H_{c1}$ using Eqs. (3) and (4) is

$$\begin{aligned} E_{\text{anis ave}} &= \frac{K_3}{3} [\sin(3\phi_A) + \sin(3\phi_B) + \sin(3\phi_C)] \\ &= -\frac{K_3}{3} [1 + 2 \cos(3\Delta\phi)]. \end{aligned} \quad (5)$$

A plot of $E_{\text{anis ave}}/K_3$ versus $\Delta\phi$ is shown in Fig. 4(a). The negative (lowest-energy) value of $E_{\text{anis ave}}/K_3$ at $\Delta\phi = 0$ is seen to become positive with increasing $\Delta\phi$.

The magnetic energy in the regime $0 \leq H_x \leq H_{c1}$ is given by

$$\begin{aligned} E_{\text{mag}} &= -M_x H_x = -[\chi_\perp H_x \sin(\phi)] H_x \\ &= -\chi_\perp H_x^2 \sin(\phi), \end{aligned} \quad (6a)$$

where $\chi_x \equiv \chi_\perp = M_x/H_x$ is the ab -plane magnetic susceptibility at $T = 0$ when all moments are perpendicular to \mathbf{H}_x , *i.e.*, when $\phi = \pi/2$. Summing over the angles of the moments in the three domains in Eq. (4) and dividing by 3 gives the average magnetic energy as

$$E_{\text{mag ave}} = -\frac{\chi_\perp H_x^2}{3} \left[1 + 2 \sin^2 \left(\frac{\pi}{6} + \Delta\phi \right) \right]. \quad (6b)$$

The total average energy is $E_{\text{ave}} = E_{\text{anis ave}} + E_{\text{mag ave}}$, which is given by Eqs. (5) and (6b) as

$$\begin{aligned} E_{\text{ave}} &= -\frac{K_3}{3} [1 + 2 \cos(3\Delta\phi)] \\ &\quad -\frac{\chi_\perp H_x^2}{3} \left[1 + 2 \sin^2 \left(\frac{\pi}{6} + \Delta\phi \right) \right]. \end{aligned} \quad (7a)$$

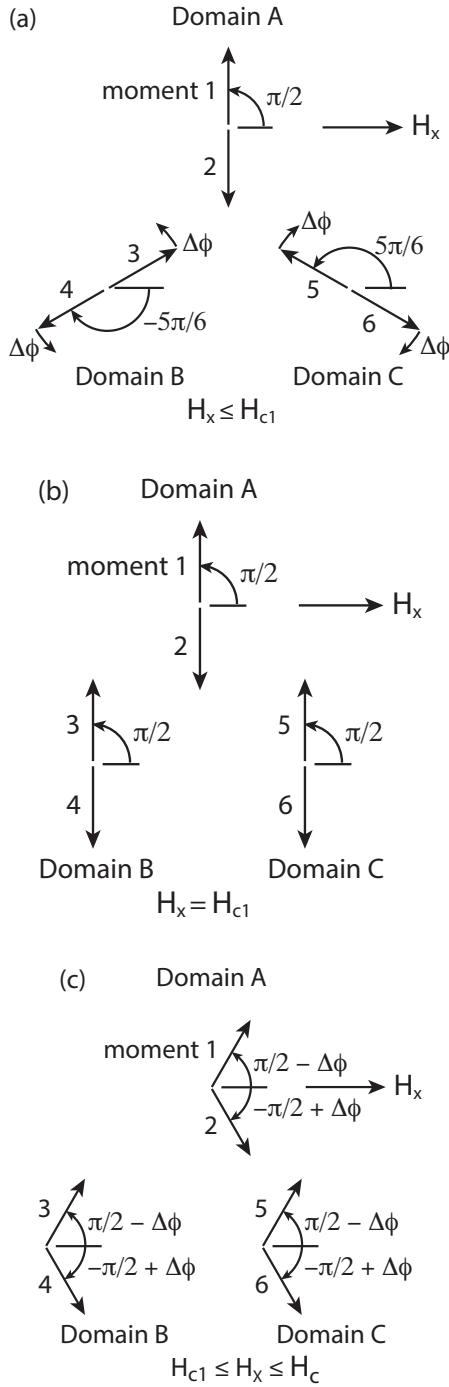


FIG. 3. (a) Reorientation of the Eu magnetic moments in the three trigonal antiferromagnetic domains in a small ab -plane magnetic field $H_x < H_{c1}$. The arrows indicate the direction and increment $\Delta\phi$ of rotation of the moments in domains B and C towards the vertical orientation. The moments in each domain remain antiparallel to each other for $H_x < H_{c1}$ apart from a small canting towards the magnetic field direction ($\lesssim 1^\circ$) that gives rise to the measured magnetization. (b) Orientation of the moments at the critical field $H_x = H_{c1}$ where all moments are perpendicular to H_x except for the small canting towards H_x . (c) Canting of all moments toward H_x for $H_{c1} < H_x < H_c$. At the critical field H_c all moments are aligned ferromagnetically in the direction of \mathbf{H}_x .

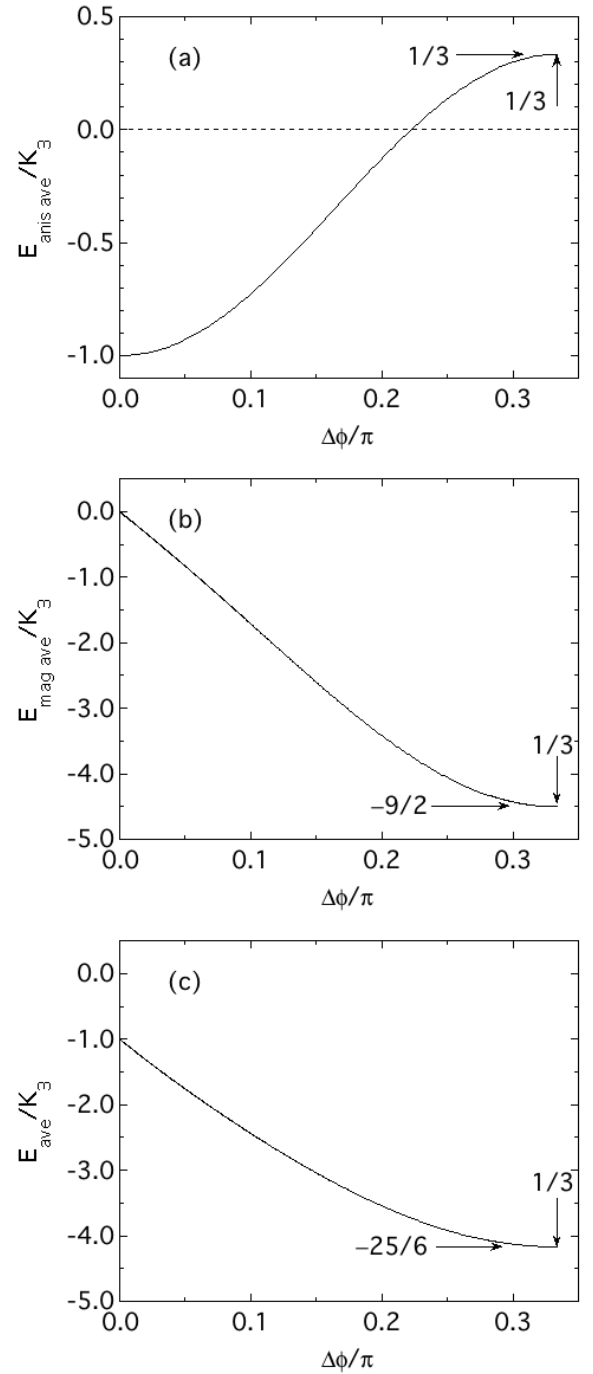


FIG. 4. (a) Average anisotropy energy $E_{\text{anis,ave}}$, (b) average magnetic energy $E_{\text{mag,ave}}$, and (c) the average total energy E_{ave} , all normalized by the anisotropy constant K_3 , versus the tilt angle $\Delta\phi/\pi$ of the AFM moments in Fig. 3(a) except for the moments in Domain A for which $\Delta\phi = 0$. The value $|\Delta\phi|/\pi = 1/3$ occurs at $H_x = H_{c1}$.

In order to minimize E_{ave} with respect to $\Delta\phi$ at each value of H_x with $0 \leq H_x \leq H_{c1}$, we first normalize the average energy in Eq. (7a) by K_3 , yielding

$$\frac{E_{\text{ave}}}{K_3} = -\frac{1}{3} \left\{ 1 + 2 \cos(3\Delta\phi) + \frac{\chi_{\perp}}{K_3} H_x^2 \left[1 + 2 \sin^2 \left(\frac{\pi}{6} + \Delta\phi \right) \right] \right\}, \quad (7b)$$

where both sides of the equation in cgs units are dimensionless since the cgs units of χ_{\perp} are cm^3 , those of H_x^2 are erg/cm^3 , and those of K_3 are ergs. Minimizing E_{ave}/K_3 with respect to the quantity $\chi_{\perp} H_x^2/K_3$ yields $\Delta\phi$ versus $\chi_{\perp} H_x^2/K_3$ as plotted in Fig. 5. Then using the data in the figure for the last point on the right end of the plot at $H = H_{c1}$ for which $\Delta\phi = \pi/3$, we obtain

$$\frac{\chi_{\perp} H_{c1}^2}{K_3} = \frac{9}{2}. \quad (8a)$$

We calculated the value of the constant on the right-hand side of Eq. (8a) to high precision, and it appears to be exact. Equation (8a) gives

$$\frac{\chi_{\perp}}{K_3} = \frac{9/2}{H_{c1}^2}. \quad (8b)$$

Inserting this expression into Eqs. (6b) and (7b) respectively gives

$$\frac{E_{\text{mag ave}}}{K_3} = -\frac{3}{2} \left(\frac{H_x}{H_{c1}} \right)^2 \left[1 + 2 \sin^2 \left(\frac{\pi}{6} + \Delta\phi \right) \right] \quad (9a)$$

and

$$\frac{E_{\text{ave}}}{K_3} = -\frac{1}{3} \left\{ 1 + 2 \cos(3\Delta\phi) + \frac{9}{2} \left(\frac{H_x}{H_{c1}} \right)^2 \left[1 + 2 \sin^2 \left(\frac{\pi}{6} + \Delta\phi \right) \right] \right\}. \quad (9b)$$

A plot of $E_{\text{mag ave}}/K_3$ versus $\Delta\phi$ for $0 \leq H_x \leq H_{c1}$ is shown in Fig. 4(b) and a corresponding plot of E_{ave}/K_3 versus $\Delta\phi$ is shown in Fig. 4(c). For E_{ave}/K_3 , the minimum energy is obtained at $\Delta\phi = \pi/3$ for which the moments in all three domains are perpendicular to H_x apart from the slight canting towards H_x discussed above that gives rise to the observed magnetization versus H_x .

For $0 \leq H_x \leq H_{c1}$, the magnetization M_x of the two collinear moments in a domain at $T = 0$ versus H_x only arises from the perpendicular component of \mathbf{M} , because the parallel component gives no contribution at $T = 0$ K. The normalized magnetization averaged over the three domains using Eqs. (4) is

$$\begin{aligned} \frac{M_{x \text{ ave}}}{M_x(H_{c1})} &= \frac{1}{3} \left[\sin^2(\phi_A) + \sin^2(\phi_B) + \sin^2(\phi_C) \right] \\ &= \frac{1}{3} \left[1 + 2 \sin^2 \left(\frac{\pi}{6} + \Delta\phi \right) \right]. \end{aligned} \quad (10)$$

Thus if $\Delta\phi = 0$, $M_{x \text{ ave}}/M_x(H_{c1}) = 1/2$, whereas if $\Delta\phi = \pi/3$, all the moments are perpendicular to H_x ,

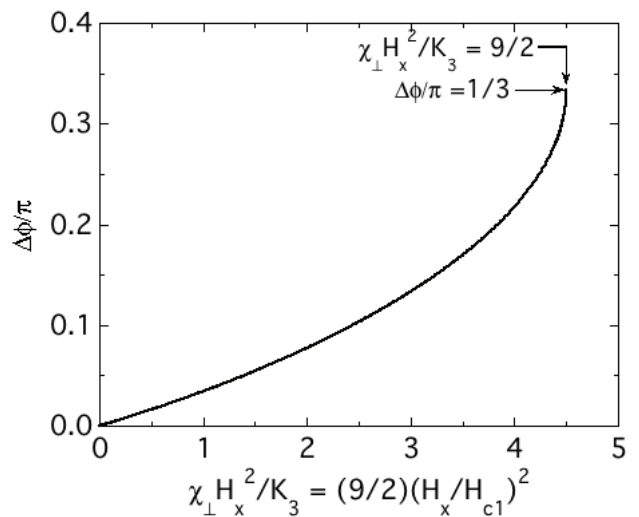


FIG. 5. The angle $\Delta\phi/\pi$ in Fig. 3(a) versus $\chi_{\perp} H_x^2/K_3$ in Eqs. (7). The alternate abscissa label is obtained using Eq. (8b).

giving the maximum value $M_{x \text{ ave}}/M_x(H_{c1}) = 1$ for the locked moments in the three domains. A plot of $M_{x \text{ ave}}/M_x(H_{c1})$ versus $\Delta\phi/\pi$ over the relevant range $0 \leq \Delta\phi/\pi \leq 1/3$ is shown in Fig. 6.

C. $H_{c1} \leq H_x \leq H_{ab}^c$

When $H_{c1} \leq H_x \leq H_{ab}^c$, where H_{ab}^c is the critical field at which $M_x \equiv M_{ab}$ reaches saturation at $7 \mu_B/\text{Eu}$, the magnetization is due to canting of the moments towards H_x in each domain as illustrated in Fig. 3(c). In this regime, $M_x \propto H_x$ as seen at the higher fields in Fig. 1. Combining the previous results, a plot of the calculated $M_x(H_x)/M_x(H_{c1})$ versus H_x/H_{c1} is shown in Fig. 7. This plot looks similar to the experimental data for EuMg_2Bi_2 and EuMg_2Sb_2 in Fig. 1. In the following section we obtain an expression for K_3 and its respective values for EuMg_2Bi_2 and EuMg_2Sb_2 .

IV. FITS TO THE LOW- T MAGNETIZATION DATA FOR EuMg_2Bi_2 AND EuMg_2Sb_2

A. Determining and interpreting the experimental value of H_{c1} from $M(H_x)$ data at $T \ll T_N$

According to Fig. 7, H_{c1} can be found from the experimental $M(H_x)$ data by calculating $dM(H_x)/dH_x$ versus H_x and identifying the magnetic field at which the peak occurs as H_{c1} . Then using the measured value of H_{c1} and the molar χ_{\perp} which is the molar magnetic susceptibility in the ab plane at T_N within MFT, the value of the anisotropy constant K_3 can be calculated. The value of K_3 per formula unit (f.u.) (per Eu atom in our case) is

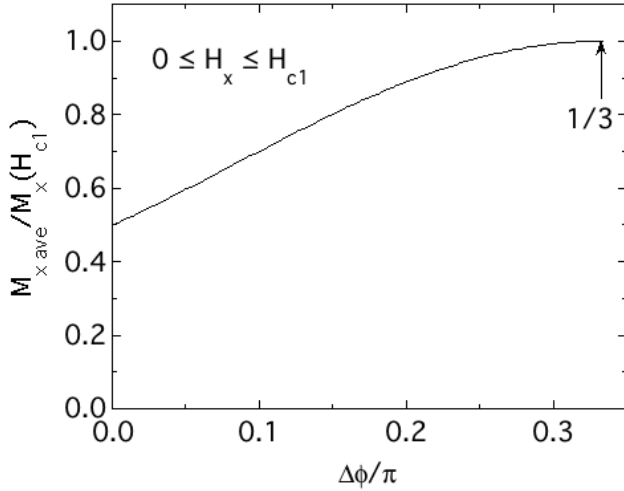


FIG. 6. Average magnetization $M_{x\text{ave}}$ in the direction of the field H_x normalized by $M_x(H_{c1})$ versus the angle $\Delta\phi/\pi$ of the AFM domains in Fig. 3(a), where the angle $\Delta\phi/\pi = 1/3$ corresponds to the field $H_x = H_{c1}$.

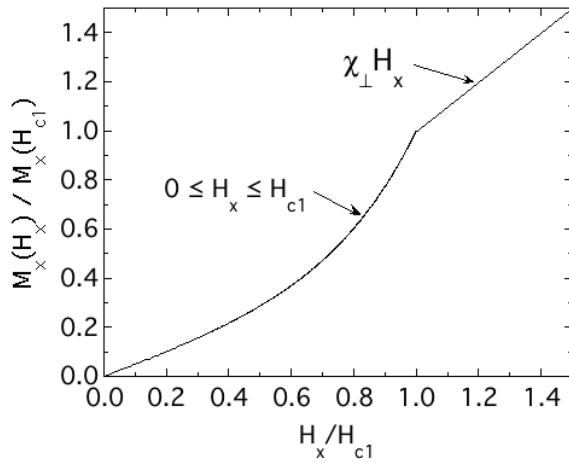


FIG. 7. Theoretical magnetization ratio $M_x(H_x)/M_x(H_{c1})$ vs the field ratio H_x/H_{c1} . Above H_{c1} , this ratio vs H_x/H_{c1} is linear, which continues up to the critical field ratio H_{c1}^c/H_{c1} , above which the ratio remains constant. Here χ_{\perp} is the magnetic susceptibility along the x axis in the ab plane that is perpendicular to the moments at $H_x = H_{c1}$ in Fig. 3(b).

obtained from Eq. (8a) as

$$K_3 = \frac{\chi_{\perp} H_{c1}^2}{(9/2)N_A}, \quad (11)$$

where $\chi_{\perp} = \chi_{ab}$, N_A is Avogadro's number, $\chi(T_N)$ is in cgs units of cm^3/mol , and H_{c1} is in cgs units of $\text{Oe} = \text{G}$ (Gauss). Using the cgs units of $\chi_{ab}(T_N)$ given by $\text{cm}^3/\text{mol f.u.}$, the conversion factor $1 \text{ G}^2 = 1 \text{ erg}/\text{cm}^3$, and the units $1/\text{mol}$ of N_A , the cgs units of K_3 are $\text{erg}/\text{f.u.} = 1.602 \times 10^{-12} \text{ eV}/\text{f.u.}$

B. Modeling the experimental $M_{ab}(H)$ data at $T = 1.8 \text{ K}$ for EuMg_2Bi_2 and EuMg_2Sb_2

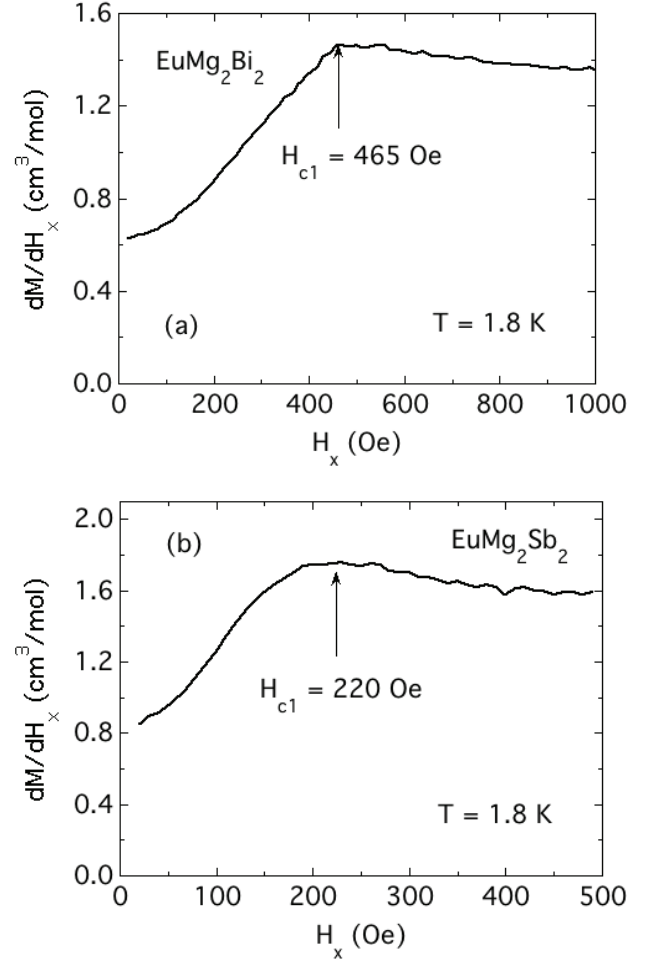


FIG. 8. Magnetic field derivative dM/dH_x vs $H_x (= H_{ab})$ of the $M_x(H_x)$ data for EuMg_2Bi_2 and EuMg_2Sb_2 in Figs. 1(a) and 1(b), respectively, in the low-field region from which the critical fields $H_{c1} \approx 465$ and ≈ 220 Oe are obtained, respectively. The high-field behavior eventually asymptotes to the respective ab -plane magnetic susceptibilities $\chi_{ab}(T_N) = 1.31$ and $1.54 \text{ cm}^3/\text{mol}$, respectively.

Figures 8(a) and 8(b) show the derivative dM/dH_x vs H_x in the ab plane for EuMg_2Bi_2 and EuMg_2Sb_2 obtained from the data in Figs. 1(a) and 1(b), respectively. The data exhibit maxima in dM/dH_x which yield $H_{c1} = 465$ Oe for EuMg_2Bi_2 and 220 Oe for EuMg_2Sb_2 , respectively. Then using the value $\chi_{ab}(T_N) = 1.31 \text{ cm}^3/\text{mol}$ from Fig. 5(a) of Ref. [6] which is the same as the value of the high-field derivative at $H_{c1} \approx 465$ Oe in Fig. 8(a), the value of K_3 is obtained from Eq. (11) for EuMg_2Bi_2 . Similarly, for EuMg_2Sb_2 $\chi_{ab}(T_N) = 1.58 \text{ cm}^3/\text{mol}$ and $H_{c1} \approx 220$ Oe. The results for the respective trigonal

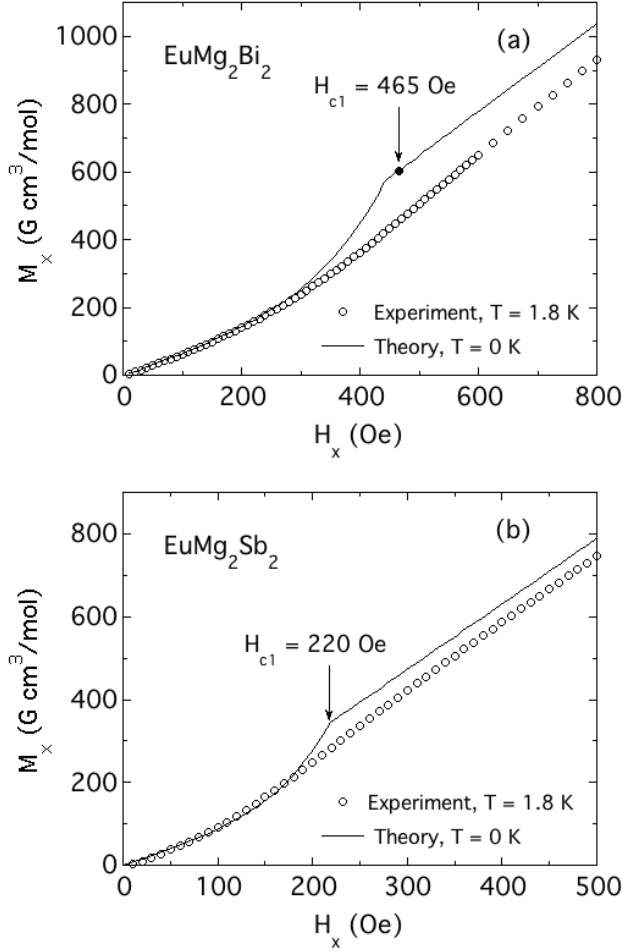


FIG. 9. Experimental magnetization $M_x = M_{ab}$ versus magnetic field $H_x = H_{ab}$ at $T = 1.8$ K (open circles) and the theoretical predictions for $T = 0$ K (solid curve) for (a) EuMg_2Bi_2 with $H_{c1} \approx 465$ Oe and (b) EuMg_2Sb_2 with $H_{c1} \approx 220$ Oe.

anisotropy constants are

$$K_3 = 1.0 \times 10^{-19} \text{ erg/Eu} \quad (\text{EuMg}_2\text{Bi}_2) \quad (12a)$$

$$= 6.5 \times 10^{-8} \text{ eV/Eu},$$

$$K_3 = 2.8 \times 10^{-20} \text{ erg/Eu} \quad (\text{EuMg}_2\text{Sb}_2) \quad (12b)$$

$$= 1.8 \times 10^{-8} \text{ eV/Eu}.$$

Thus the trigonal anisotropy constant K_3 in EuMg_2Sb_2 is significantly smaller than in EuMg_2Bi_2 .

Comparisons of the experimental $M_{ab}(H)$ data at $T = 1.8$ K for EuMg_2Bi_2 in Fig. 1(a) and EuMg_2Sb_2 in Fig. 1(b) with the theoretical predictions at $T = 0$ K using the experimental values of H_{c1} and $M_x(H_{c1})$ are shown in Figs. 9(a) and 9(b), respectively. The theory accurately describes the experimental data below H_{c1} and the slope of the data above H_{c1} , but the latter prediction is displaced upwards from the experimental data for both compounds. We speculate that this difference arises from the finite temperature 1.8 K of the measurements, which is a significant fraction of $T_N = 6.7$ K for EuMg_2Bi_2 and

$T_N = 8.0$ K for EuMg_2Sb_2 , compared with $T = 0$ K for the theory.

C. Theoretical anisotropy values

1. Magnetic Dipole and Critical-Field Anisotropies

The energy of interaction E_i of a magnetic moment μ_i due to the magnetic dipole interaction (MDI) with the other identical moments in a magnetically-ordered crystal is given by [22]

$$E_{i\alpha} = -\epsilon\lambda_{k\alpha}, \quad (13a)$$

with

$$\epsilon = \frac{\mu^2}{2a^3}. \quad (13b)$$

The $\lambda_{k\alpha}$ values are the eigenvalues of the dimensionless symmetric MDI tensor, where k is the magnetic propagation vector and α is the ordered-moment axis $\hat{\mu}$. The ordered magnetic moments are described by $\vec{\mu}_i = \mu\hat{\mu}_i$, and a is the basal-plane lattice parameter of the respective crystal structure.

a. EuMg_2Bi_2 For $c/a = 1.644$ [6] and the A-type AFM propagation vector $(0,0,\frac{1}{2})$ r.l.u. [7], the MDI tensor eigenvalues for the three Cartesian ordered-moment axes are $\lambda_{[100]} = 5.515488367755699$, $\lambda_{[010]} = 5.515488367755807$ using high-precision calculations, and $\lambda_{[001]} = -11.0386$. The in-plane anisotropy energy ΔE per formula unit of EuMg_2Bi_2 is given by

$$\Delta E = -\epsilon(\lambda_{[100]} - \lambda_{[010]}), \quad (14)$$

where the moment directions are in Cartesian coordinates with the a axis designated by $[100]$ and a direction perpendicular to it in the ab plane by $[010]$. This would correspond to the amplitude of oscillation of the anisotropy energy in Fig. 2. Using the values $a = 4.7724 \times 10^{-8}$ cm and $\mu = 7 \mu_B$ [7, 8], we obtain $\Delta E = 3.00956 \times 10^{-18}$ eV/Eu. This value is a factor of 10^{10} smaller than estimated for K_3 in Eq. (12a). As a reference point, taking $\mu = 7 \mu_B$ and $H_{c1} = 465$ Oe gives $\mu H_{c1} = 1.88 \times 10^{-5}$ eV. Thus the in-plane anisotropy energy associated with in-plane locked-moment reorientation in the AFM domains in Fig. 3(a) must arise from a source other than the magnetic-dipole interaction.

The magnetic-dipole anisotropy energy difference between the observed ab plane and c axis ordering is

$$\Delta E = -\epsilon(\lambda_{[100]} - \lambda_{[001]}) \quad (15a)$$

$$= -0.2004 \text{ meV}. \quad (15b)$$

The equivalent magnetic anisotropy field ΔH is

$$\Delta H = \frac{\Delta E}{\mu} = -4945 \text{ Oe}. \quad (15c)$$

Thus, ab -plane ordering in the A-type AFM state of EuMg_2Bi_2 is favored over c -axis ordering associated with

magnetic-dipole interactions, as observed. This is consistent with the critical fields H^c at $T = 1.8$ K obtained from $M(H)$ isotherms $H_c^c = 40(3)$ kOe and $H_{ab}^c = 27.5(2)$ kOe [6], yielding $H_c^c - H_{ab}^c \approx 12,000$ Oe. This is because it is easier to cant the moments in each domain towards an ab -plane field than it is to cant them along the c axis according to Eqs. (15). On the other hand, this difference in critical fields is significantly larger than the magnitude of ΔH in Eq. (15c), suggesting the presence of a source of ΔH in addition to the magnetic-dipole interaction.

b. EuMg₂Sb₂ The corresponding magnetic-dipole calculations for EuMg₂Sb₂ are given in the Appendix of Ref. [8]. At 6.6 K, the lattice parameters are $a = 4.5431$ Å, $c = 7.6668$ Å, $c/a = 1.6477$. The results for A-type AFM ordering are

$$\lambda_{[100]} = 5.519 \quad (\text{a axis ordering}) \quad (16a)$$

$$\lambda_{[001]} = -11.038 \quad (\text{c axis ordering}) \quad (16b)$$

$$\lambda_{[100]} - \lambda_{[001]} = 16.557 \quad (16c)$$

$$\Delta E = -0.2162 \text{ meV} \quad (16d)$$

$$\Delta H = -5334 \text{ Oe.} \quad (16e)$$

At $T = 1.8$ K, the measured critical fields are $H_c^c = 34(1)$ kOe and $H_{ab}^c = 26(1)$ kOe, yielding $H_c^c - H_{ab}^c \approx 8.0$ kOe, which indicates that the magnetic-dipole interaction is an important source of magnetic anisotropy in EuMg₂Sb₂, as in EuMg₂Bi₂.

The experimental results are summarized in Table I.

2. Magnetocrystalline Anisotropy Energy (MCAE) from Density-Functional Theory

Table II summarizes the calculated DFT energy, magnetic-dipole energy (MDE), and total energy for four different magnetic configurations in EuMg₂Bi₂ and EuMg₂Sb₂. Two observations are consistent with experiments: (1) The A-type AFM with an in-plane spin orientation has the lowest total energies calculated in both compounds; (2) EuMg₂Bi₂ has a larger easy-plane anisotropy than EuMg₂Sb₂. The magnetic anisotropy (MA, K_{Total}) contains two contributions: MDA and the SOC-originated MCA. The Eu-4*f* shell is half-filled in these compounds, resulting in a large spin moment of $\sim 7 \mu_B/\text{Eu}$ and a negligible orbital moment. Rotating the roughly spherical Eu-4*f* charge cloud in a crystal field costs little energy, resulting in a relatively small MCA compared to typical rare-earth-based magnets with open 4*f*-shell orbitals. On the other hand, the large Eu spin moment gives considerable MDE and corresponding MDA. For example, for the ground-state A-type ordering, K and K_D are 0.1255 and 0.2004 meV/Eu, respectively, in EuMg₂Bi₂ while the values are 0.038 and 0.2162 meV/Eu, respectively, in EuMg₂Sb₂. The MDE and K_D are similar in two compounds as they share similar lattice parameters and Eu magnetic on-site moments. Thus, K_D dominates the easy-plane MA for the A-type

AFM ground state, especially in EuMg₂Sb₂, where the MCA is weaker. On the other hand, the larger easy-plane MA in EuMg₂Bi₂ is due to its larger MCA.

Besides the easy-plane anisotropy, we also calculated the in-plane MCAE by varying the spin orientation within the ab plane; the obtained energy difference is smaller than 2×10^{-7} eV/Eu. This result is consistent with Eqs. (12) which indicate that the in-plane anisotropy energies are $K_3 = 1.8$ and 6.5×10^{-8} eV/Eu for EuMg₂Sb₂ and EuMg₂Bi₂, respectively. Thus an accurate estimation of the small in-plane MCAE is beyond the resolution of the present DFT approach. As noted previously, the in-plane MDAE is negligible.

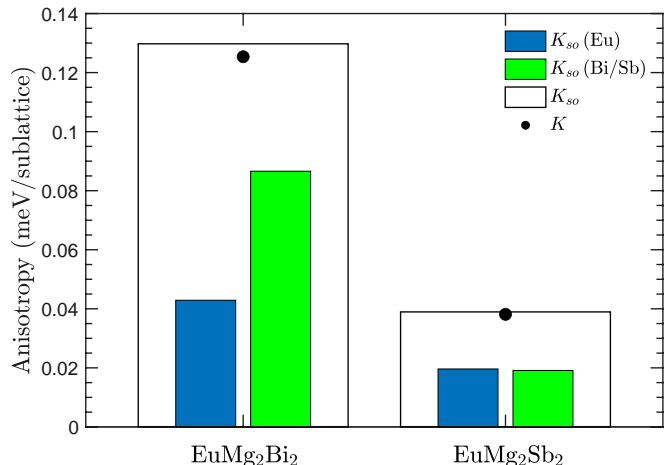


FIG. 10. Total and sublattice-resolved anisotropy of spin-orbit-coupling energy K_{so} , defined as in Eq. (2), in A-type AFM EuMg₂Bi₂ and EuMg₂Sb₂. Magnetocrystalline anisotropy energy (MCAE) K is also shown (black dots) and agrees well with total K_{so} (black box). The MCAE is calculated according to Eq. (1) using the total energies. The K_{so} contribution from Mg sublattice $K_{so}(\text{Mg})$ is negligible and not shown.

a. Origin of easy-plane MCA The larger easy-plane MCA in EuMg₂Bi₂ than in EuMg₂Sb₂ can be understood by resolving the anisotropy of SOC energy K_{so} into sublattices [14, 17]. Although the MCA is generally associated with the Eu spin's alignment, it also depends on the nature of the other constituent atoms in the compound. Figure 10 shows the sublattice-resolved and total K_{so} , compared with MCAE K . The difference between the total K_{so} and K is within 4% in both compounds. Within perturbation theory, K_{so} is proportional to the difference between spin-parallel and spin-flip components of the orbital susceptibilities, vanishing in the nonmagnetic limit [15]. The strongly-magnetic Eu atoms spin-polarize the otherwise nonmagnetic Bi/Sb atoms, inducing sizable K_{so} on the Bi and Sb sublattices. The $K_{so}(\text{Bi})$ in EuMg₂Bi₂ is larger than the $K_{so}(\text{Sb})$ in EuMg₂Sb₂, which is likely due to the larger Bi-*p* SOC constant (~ 2 eV) than that of Sb-*p* (~ 0.74 eV). Furthermore, the $K_{so}(\text{Eu})$ is larger in EuMg₂Bi₂ than in EuMg₂Sb₂. On the other hand, the light Mg atom has

TABLE I. Summary of experimental data for EuMg_2Bi_2 and EuMg_2Sb_2 . Listed for each compound are the hexagonal lattice parameters a , c , and c/a , the value $\epsilon = \mu^2/(2a^3)$ in Eq. (13b) where the Eu moment is $\mu = 7\mu_B$, the Néel temperatures T_N , and the critical fields H_{c1} , H_{ab}^c , and H_c^c . Except for H_{c1} obtained in the text, the values cited are from Refs. [6, 8]. The abbreviation RT stands for room temperature.

Compound	a (Å)	c (Å)	c/a	ϵ (meV)	T_N (K)	H_{c1} (Oe)	H_{ab}^c (kOe)	H_c^c (kOe)
EuMg_2Bi_2	4.7724(3) (RT)	7.8483(5) (RT)	1.6445(2) (RT)	0.01210	6.7(1)	465(2)	27.5(2)	40(3)
EuMg_2Sb_2	4.6861(3) (RT)	7.7231(5) (RT)	1.6481(2) (RT)		8.0(2)	220(10)	26(1)	34(1)
	4.6531(5) (6.6 K)	7.6668(5) (6.6 K)	1.6477(3) (6.6 K)	0.01306				

TABLE II. Theoretical data for EuMg_2Bi_2 and EuMg_2Sb_2 . Here, \mathbf{k} is the propagation vector of the ordering in reciprocal-lattice units (r.l.u.) and $\vec{\alpha}$ is the collinear polarization of the ordered moments in real space. For each magnetic configuration, the two arrows in the second column represent the spin orientations of two neighboring Eu layers. The magnetic-dipole energy (MDE) is calculated using the results in Ref. [22]. The DFT energy calculated with spin-orbit coupling is also listed for both ferromagnetic (FM) and A-type antiferromagnetic (AFM) ordering, each for both ab -plane and c -axis moment alignment. The total energy is calculated as the sum of MDE and DFT energy. The MDE per moment is calculated from the ϵ values in Table I and the $\lambda_{\mathbf{k},\alpha}$ values using Eqs. (13) in the text. All MDE calculations assume the Eu moment of $m_{\text{Eu}} = 7\mu_B$ and neglect the small induced moments on Bi/Sb and Mg sites. For DFT energy and total energy, the ground-state values are chosen as reference zero. Due to the negative sign in Eq. (13a), the most probable magnetic structure in the second column for each compound due to MDE alone is the one with the largest positive value of $\lambda_{\mathbf{k},\alpha}$ in the sixth column and hence the most negative value in the eighth column. The magnetic anisotropy energy (MAE) contains two contributions: magnetocrystalline anisotropy energy (MCAE) and magnetic-dipole anisotropy energy (MDAE). They are listed for both A-type AFM and FM ordering as the corresponding energies of the c -axis moment alignment above those of the ab -plane moment alignment. All energies listed here are in units of meV/Eu.

Compound	Configuration	Ordering	\mathbf{k} (r.l.u.)	$\vec{\alpha}$	$\lambda_{\mathbf{k},\alpha}$	DFT Energy	MDE	Total Energy	MCAE	MDAE	MAE
EuMg_2Bi_2	$\rightarrow\leftarrow$	A-type AFM	(0,0,1/2)	[1 0 0]	5.519	0	-0.0668	0	0.1255	0.2004	0.3259
	$\rightarrow\rightarrow$	FM	(0,0,0)	[1 0 0]	2.571	1.6195	-0.0311	1.6552	0.0205	0.0934	0.1139
	$\uparrow\downarrow$	A-type AFM	(0,0,1/2)	[0 0 1]	-11.038	0.1255	0.1336	0.3259			
	$\uparrow\uparrow$	FM	(0,0,0)	[0 0 1]	-5.142	1.6400	0.0623	1.7691			
EuMg_2Sb_2	$\rightarrow\leftarrow$	A-type AFM	(0,0,1/2)	[1 0 0]	5.519	0	-0.0721	0	0.0380	0.2162	0.2542
	$\rightarrow\rightarrow$	FM	(0,0,0)	[1 0 0]	2.577	1.2775	-0.0337	1.3159	0.0265	0.1011	0.1276
	$\uparrow\downarrow$	A-type AFM	(0,0,1/2)	[0 0 1]	-11.038	0.0380	0.1441	0.2542			
	$\uparrow\uparrow$	FM	(0,0,0)	[0 0 1]	-5.155	1.3040	0.0674	1.4435			

a very small SOC constant and negligible K_{so} . We note that such an MA mechanism that combines the strongly-magnetic $3d$ (or here $4f$) elements with the large-SOC heavy- p elements is also responsible for the MA in many other systems, such as the two-dimensional van der Waals materials CrI_3 , MnBi_2Te_4 , and MnSb_2Te_4 [23–25]. Similarly, MnBi_2Te_4 has been found to have a much larger MCA than MnSb_2Te_4 [24].

b. Anisotropic exchange Since the K_{so} s of Bi/Sb contribute significantly to MCA and exist only when they are spin-polarized by neighboring Eu atoms, one may expect that the $K_{\text{so}}(\text{Bi/Sb})$ and total K depend on the magnetic structure of the Eu moments. Indeed, we found a large difference in the MCA between A-type and FM ordering in EuMg_2Bi_2 . This difference suggests that the MCA contains terms beyond single-ion terms when mapping the total energy into the effective magnetic Hamiltonian that includes only the Eu sites. We map the energies of the four configurations listed in Table II into the

TABLE III. Coefficients (C) of the isotropic interlayer exchange J_c , anisotropic interlayer exchange γ_c , and single-ion anisotropy A for the four different spin configurations when mapped onto the spin Hamiltonian defined in Eq. (17). The four configurations and their energies are detailed in Table II. The three columns on the right in the present table represent the differences of the coefficients with respect to the ground state ($\rightarrow\leftarrow$), where $\Delta C = C - C^{\rightarrow\leftarrow}$.

Configuration	C			ΔC		
	J_c	γ_c	A	J_c	γ_c	A
$\rightarrow\leftarrow$	-2	0	0	0	0	0
$\rightarrow\rightarrow$	2	0	0	4	0	0
$\uparrow\downarrow$	-2	-2	1	0	-2	1
$\uparrow\uparrow$	2	2	1	4	2	1

Hamiltonian

$$H = \sum_{i \neq j} J_c \hat{\mathbf{e}}_i \cdot \hat{\mathbf{e}}_j + \sum_{i \neq j} \gamma_c (\hat{\mathbf{e}}_i^z \hat{\mathbf{e}}_j^z) + \sum_i A_i (\hat{\mathbf{e}}_i^z)^2, \quad (17)$$

where J_c and γ_c are the effective isotropic and anisotropic interlayer exchanges, respectively, A is the single-ion anisotropy, and $\hat{\mathbf{e}}_i$ is the unit vector of the Eu magnetic moment at site i . The coefficients C of J_c , γ_c , and A for the four magnetic structures in Table II are listed in Table III. The three effective interactions can be written as

$$\begin{pmatrix} J_c \\ \gamma_c \\ K \end{pmatrix} = \begin{pmatrix} 4 & 0 & 0 \\ 0 & -2 & 1 \\ 4 & 2 & 1 \end{pmatrix}^{-1} \begin{pmatrix} E_{\rightarrow\rightarrow} \\ E_{\uparrow\downarrow} \\ E_{\uparrow\uparrow} \end{pmatrix}. \quad (18)$$

Using Eq. (18) and the DFT energy values listed in Table II, we obtain $J_c = 0.405(0.32)$ meV/Eu, $\gamma_c = -0.026(-0.003)$ meV/Eu, and $A = 0.073(0.032)$ meV/Eu in EuMg₂Bi₂ (EuMg₂Sb₂), indicating a significant anisotropic exchange γ_c in EuMg₂Bi₂.

V. CONCLUDING REMARKS

Our previous measurements of the in-plane magnetization $M(H_x)$ at low T (1.8 K) of trigonal EuMg₂Bi₂ and EuMg₂Sb₂, which is below T_N of each compound, exhibited positive curvature for $H_x \lesssim 200$ –500 Oe followed by a proportional behavior up to the respective critical field H_{ab}^c [6, 7]. Here we formulated a theory which quantitatively explains these results. Due to the threefold trigonal magnetic anisotropy of each compound shown in Fig. 3(a), the A-type AFM ordering leads to three collinear AFM domains at 120° to each other. In an applied field H_x in the ab plane, the ordered moments in each domain rotate with increasing field to become approximately perpendicular to \mathbf{H}_x at a critical field $H_{c1} \approx 220$ Oe for EuMg₂Sb₂ and ≈ 465 Oe for EuMg₂Bi₂ as illustrated in Fig. 3(b). Then on further increasing H_x , the moments all tilt towards \mathbf{H}_x in such a way that $M(H_x)$ is linear in H_x as shown in Fig. 3(c) until all moments are parallel to the field at the critical

field H_{ab}^c which is 26 kOe for EuMg₂Sb₂ and 27.5 kOe for EuMg₂Bi₂.

Magnetic-dipole calculations showed that ab -plane ordered-moment alignment is strongly favored over c -axis alignment. From the values of H_{c1} , our theory allowed us to determine the in-plane trigonal anisotropy constant $K_3 = 1.8 \times 10^{-8}$ eV/Eu for EuMg₂Sb₂ and $K_3 = 6.5 \times 10^{-8}$ eV/Eu for EuMg₂Bi₂. The in-plane magnetic anisotropy due to magnetic dipole interactions is found to be far too small to account for the observed values of K_3 , and hence must arise from an alternate mechanism. However, the K_3 values are below the resolution of our DFT calculations. On the other hand, our DFT calculations of the magnetocrystalline anisotropy energy including spin-orbit coupling showed XY anisotropy resulting in ab -plane magnetic ordering with A-type antiferromagnetic ordering favored over ferromagnetic ordering. Furthermore, anisotropic exchange between the Eu spins was found to be significant in EuMg₂Bi₂.

An interesting avenue for future work is to calculate the temperature dependence of the in-plane magnetization $M(H_x)$ up to the respective T_N of EuMg₂Sb₂ and EuMg₂Bi₂ for comparison with the corresponding data in Refs. [6, 7]. Another avenue is to investigate the low ab -plane field behavior of A-type-antiferromagnets with a layered tetragonal Eu structure and with the ordered moments in the ab plane which would have twofold in-plane anisotropy instead of the threefold trigonal in-plane anisotropy in EuMg₂Sb₂ and EuMg₂Bi₂.

ACKNOWLEDGMENTS

We thank Robert McQueeney, Benjamin Ueland, and David Vakhnin for helpful discussions. This research was supported by the U.S. Department of Energy, Office of Basic Energy Sciences, Division of Materials Sciences and Engineering. Ames Laboratory is operated for the U.S. Department of Energy by Iowa State University under Contract No. DE-AC02-07CH11358.

-
- [1] F. Wartenberg, C. Kranenberg, R. Pocha, D. Johrendt, A. Mewis, R.-D. Hoffmann, B. D. Mosel, and R. Pöttgen, Neue Pnictide im CaAl₂Si₂-Typ und dessen Existenzgebiet, *Z. Naturforsch.* **57b**, 1270 (2002).
- [2] M. Marshall, I. Pletikocić, M. Yahyavi, H.-J. Tien, T.-R. Chang, H. Cao, and W. Xie, *J. Appl. Phys.* **129**, 035106 (2021).
- [3] A. F. May, M. A. McGuire, D. J. Singh, R. Custelcean, and G. E. Jellison, Jr., Structure and Properties of Single Crystalline CaMg₂Bi₂, EuMg₂Bi₂, and YbMg₂Bi₂, *Inorg. Chem.* **50**, 11127 (2011).
- [4] F. Kabir, M. Mofazzel Hosen, F. Cheenicode-Kabeer, A. Aperis, X. Ding, G. Dhakal, K. Dimitri, C. Sims, S. Regmi, L. Persaud, K. Gofryk, P. M. Oppeneer, D. Kaczorowski, and M. Neupane, Observation of multiple Dirac states in a magnetic topological material EuMg₂Bi₂, preprint arXiv:1912.08645 (2019).
- [5] A. K. Kundu, T. Roy, S. Pakhira, Z.-B. Wu, M. Tsujikawa, M. Shirai, D. C. Johnston, A. N. Pasupathy, and T. Valla, Topological electronic structure of YbMg₂Bi₂ and CaMg₂Bi₂, *npj Quantum Mater.* **7**, 67 (2022).
- [6] S. Pakhira, M. A. Tanatar, and D. C. Johnston, Magnetic, thermal and electronic-transport properties of EuMg₂Bi₂ single crystals, *Phys. Rev. B* **101**, 214407 (2020). Note: The field direction for the $M_{ab}(H)$ measurements in Fig. 10(b) of this paper was not quite parallel to the ab plane of the crystal studied, which caused the peak in dM_{ab}/dH versus H to be at ≈ 300 Oe instead of 465 Oe in Fig. 8(a) of the present paper.

- [7] S. Pakhira, T. Heitmann, S. X. M. Ribrolles, B. G. Ueland, R. J. McQueeney, D. C. Johnston, and D. Vaknin, Zero-field magnetic ground state of EuMg_2Bi_2 , *Phys. Rev. B* **103**, 024408 (2021), and unpublished results.
- [8] S. Pakhira, F. Islam, E. O’Leary, M. A. Tanatar, T. Heitmann, R. Prozorov, A Kaminski, D. Vaknin, and D. C. Johnston, A-type antiferromagnetic order in semiconducting EuMg_2Sb_2 single crystals, *Phys. Rev. B* **106**, 024418 (2022).
- [9] D. C. Johnston, Magnetic Susceptibility of Collinear and Noncollinear Heisenberg Antiferromagnets, *Phys. Rev. Lett.* **109**, 077201 (2012).
- [10] D. C. Johnston, Unified molecular field theory for collinear and noncollinear Heisenberg antiferromagnets, *Phys. Rev. B* **91**, 064427 (2015).
- [11] D. C. Johnston, Molecular-field-theory fits to the magnetic susceptibilities of antiferromagnetic GdCu_2Si_2 , CuO , LiCrO_2 , and $\alpha\text{-CaCr}_2\text{O}_4$ single crystals below their Néel temperatures, *J. Magn. Magn. Mater.* **535**, 168062 (2021).
- [12] G. Kresse and J. Hafner, *Ab initio* molecular dynamics for liquid metals, *Phys. Rev. B* **47**, 558 (1993).
- [13] G. Kresse and J. Furthmüller, Efficient iterative schemes for *ab initio* total-energy calculations using a plane-wave basis set, *Phys. Rev. B* **54**, 11169 (1996).
- [14] V. Antropov, L. Ke, and D. Åberg, Constituents of magnetic anisotropy and a screening of spin-orbit coupling in solids, *Solid State Commun.* **194**, 35 (2014).
- [15] L. Ke and M. van Schilfgaarde, Band-filling effect on magnetic anisotropy using a Green’s function method, *Phys. Rev. B* **92**, 014423 (2015).
- [16] L. Ke, Intersublattice magnetocrystalline anisotropy using a realistic tight-binding method based on maximally localized Wannier functions, *Phys. Rev. B* **99**, 054418 (2019).
- [17] L. Ke, D. A. Kukusta, and D. D. Johnson, Origin of magnetic anisotropy in doped $\text{Ce}_2\text{Co}_{17}$ alloys, *Phys. Rev. B* **94**, 144429 (2016).
- [18] G. Kresse and D. Joubert, From ultrasoft pseudopotentials to the projector augmented-wave method, *Phys. Rev. B* **59**, 1758 (1999).
- [19] D. D. Koelling and B. N Harmon, A technique for relativistic spin-polarized calculations, *J. Phys. C* **10**, 3107 (1977).
- [20] A. B. Shick, D. L. Novikov, and A. J. Freeman, Relativistic spin-polarized theory of magnetoelastic coupling and magnetic anisotropy strain dependence: Application to $\text{Co/Cu}(001)$, *Phys. Rev. B* **56**, R14259 (1997).
- [21] S. L. Dudarev, G. A. Botton, S. Y. Savrasov, C. J. Humphreys, and A. P. Sutton, Electron-energy-loss spectra and the structural stability of nickel oxide: An LSDA+ U study, *Phys. Rev. B* **57**, 1505 (1998).
- [22] D. C. Johnston, Magnetic dipole interactions in crystals, *Phys. Rev. B* **93**, 014421 (2016). For the magnetic-dipole interactions between the moments and associated energies for A-type antiferromagnetic order of a stacked triangular lattice of magnetic moments that were inadvertently omitted in this paper, see the Appendix of Ref. [8].
- [23] E. Gordon, V. V. Mkhitarian, H. Zhao, Y. Lee, and L. Ke, Magnetic interactions and spin excitations in van der Waals ferromagnet VI_3 , *J. Phys. D: Appl. Phys.* **54** (2021).
- [24] B. Li, J.-Q. Yan, D. M. Pajerowski, E. Gordon, A.-M. Nedić, Y. Sizyuk, L. Ke, P. P. Orth, D. Vaknin, and R. J. McQueeney, Competing Magnetic Interactions in the Antiferromagnetic Topological Insulator MnBi_2Te_4 , *Phys. Rev. Lett.* **124**, 167204 (2020).
- [25] S. X. M. Ribberolles, Q. Zhang, E. Gordon, N. P. Butch, L. Ke, J.-Q. Yan, and R. J. McQueeney, Evolution of magnetic interactions in Sb-substituted MnBi_2Te_4 , *Phys. Rev. B* **104**, 064401 (2021).